

Internal shocks driven by accretion flow variability in the compact jet of the black hole binary GX 339-4

S. Drappeau,^{1,2*} J. Malzac,^{1,2} R. Belmont,^{1,2} P. Gandhi,³ S. Corbel,⁴

¹*Université de Toulouse; UPS-OMP; IRAP; Toulouse, France*

²*CNRS; IRAP; 9 Av. colonel Roche, BP 44346, F-31028 Toulouse cedex 4, France*

³*School of Physics & Astronomy, University of Southampton, Highfield, Southampton SO17 1BJ*

⁴*Laboratoire AIM (CEA/IRFU - CNRS/INSU - Université Paris Diderot), CEA DSM/IRFU/SAP, F-91191 Gif-sur-Yvette, France*

Accepted 2014 ?? ??. Received 2014 ?? ??; in original form 2014 ?? ??

ABSTRACT

In recent years, compact jets have been playing a growing role in the understanding of accreting black hole engines. In the case of X-ray binary systems, compact jets are usually associated with the hard state phase of a source outburst. Recent observations of GX 339-4 have demonstrated the presence of a variable synchrotron spectral break in the mid-infrared band that was associated with its compact jet. In the model used in this study, we assume that the jet emission is produced by electrons accelerated in internal shocks driven by rapid fluctuations of the jet velocity. The resulting spectral energy distribution (SED) and variability properties are very sensitive to the Fourier power spectrum density (PSD) of the assumed fluctuations of the jet Lorentz factor. These fluctuations are likely to be triggered by the variability of the accretion flow which is best traced by the X-ray emission. Taking the PSD of the jet Lorentz factor fluctuations to be identical to the observed X-ray PSD, our study finds that the internal shock model successfully reproduces the radio to infrared SED of the source at the time of the observations as well as the reported strong mid-infrared spectral variability.

Key words: accretion, accretion discs – black hole physics – shock waves – relativistic processes – radiation mechanisms: non-thermal – X-rays: binaries

1 INTRODUCTION

Decades after their discovery, the fine details of the mechanisms behind jet formation and its connexion to the accretion disc are still unclear. Revealing the disc-jet connexion would help answering major questions still open concerning accreting black holes of all sizes, their growth and the role they play in galaxy evolution.

Conical compact jet models have been successful in reproducing the flat, or slightly inverted radio spectra usually seen in X-ray binary sources (Corbel et al. 2000; Fender et al. 2000; Corbel & Fender 2002). However they all require a dissipation process to compensate for the adiabatic losses (Blandford & Königl 1979). One proposed process is the conversion of jet kinetic energy to internal energy through internal shocks.

Internal shock jet models have been proposed to model the multi-wavelength emission from γ -ray burst (Rees & Meszaros 1994; Daigne & Mochkovitch 1998), active galactic nuclei (Rees 1978; Spada et al. 2001; Böttcher & Dermer 2010) and microquasars (Kaiser et al. 2000; Jamil et al.

2010; Malzac 2013). One key point of these models is that their resulting spectral energy distributions (SED) are very sensitive to the shape of the assumed fluctuations of the jet velocity (Malzac 2014). Malzac (2013) has shown that internal shocks powered by flicker noise fluctuations of the bulk Lorentz factor can entirely compensate for the adiabatic expansion losses. Interestingly, the X-ray power spectrum of X-ray binaries, which traces the variability of the accretion flow in the vicinity of the compact object, is close to a flicker noise process (Lyubarskii 1997; King et al. 2004; Mayer & Pringle 2006).

GX 339-4 is a recurrent X-ray transient and is believed to harbour a black hole in a binary system with a low-mass companion star. Although the black hole mass and the system inclination angle, and distance are still unknown, they range between 5.8 and 10 M_{\odot} (Hynes et al. 2003; Muñoz-Darias et al. 2008; Shidatsu et al. 2011), 20° and 50° (Miller et al. 2006; Done & Diaz Trigo 2010; Shidatsu et al. 2011), and 6 and 15 kpc (Hynes et al. 2004; Zdziarski et al. 2004; Shidatsu et al. 2011), respectively. The source exhibits multi-wavelength variability on a broad range of timescales (Motch et al. 1982; Fender et al. 1999; Corbel et al. 2003; Dunn et al. 2008; Gandhi 2009; Casella et al. 2010; Corbel et al.

* E-mail: samia.drappeau@irap.omp.eu

2013). In addition, it also shows evidence of relativistic jets (Fender et al. 1997; Corbel et al. 2000; Markoff et al. 2003; Gandhi et al. 2008). The data we used in the present work are part of a multi-wavelength study of GX 339-4 (Cadolle Bel et al. 2011; Corbel et al. 2013), and in particular of the first mid-infrared study of the source published in Gandhi et al. (2011) and performed in 2010 March 11. GX 339-4 was observed with the *Wide-field Infrared Survey Explorer* (*WISE*; Wright et al. 2010) satellite in 4 bands (1.36×10^{13} , 2.50×10^{13} , 6.52×10^{13} and 8.82×10^{13} Hz, respectively W4, W3, W2 and W1), at 13 epochs, sampled at multiples of the satellite orbital period of 95 minutes and with a shortest sampling interval of 11 s, when *WISE* caught the source on two consecutive scans. Radio data were obtained with the *Australian Telescope Compact Array* (*ATCA*) during two days - closest to but not simultaneous with *WISE* data - on 2010 March 7 and 2010 March 14. The mean fluxes are 9.1 ± 0.1 and 9.7 ± 0.1 mJy at 5.5 and 9 GHz, respectively. X-ray data were nearly simultaneous with *WISE*, taken between epochs 12 and 13 with the *Rossi X-ray Timing Explorer* (*RXTE*) satellite. Gandhi et al. (2011) confirms the detection in the mid-infrared of a synchrotron break associated with the compact jet in GX 339-4 (Corbel & Fender 2002), and reports the first clear detection of its strong variability. This detection of the jet's intrinsic variability and the overall properties of GX 339-4 make it the perfect source to test our model.

The objective of this paper is to determine whether an internal shock jet model driven by accretion flow variability reproduces spectral and timing observations of an X-ray binary source in the hard spectral state, known to be associated with compact jets. Our work differs from previous internal shock jet models in that we use observed X-ray power spectral density (PSD) of the studied source, GX 339-4, to constrain the fluctuations of the bulk Lorentz factor γ of the ejecta constituting the jet. In Section 2, we introduce the internal shock jet model used to perform our simulations and the assumptions chosen to model the source. Section 3 and Section 4 present the spectral and timing analyses carried out during this study, and the results obtained. We conclude this paper with a discussion of these results and suggestions for future developments in Section 5.

2 INTERNAL SHOCK MODEL

Malzac (2014) presents a newly developed numerical code which simulates the hierarchical merging and the emission of ejecta constituting a jet. In this model, a new shell of gas is ejected at each time step Δt , comparable to the dynamical timescale at r_{dyn} , the initial radius of the ejecta. The Lorentz factor of each created shell varies, depending on the time of ejection. Its fluctuation follows a specified PSD shape. Throughout the duration of the simulation, the injected shells - and any subsequent shells resulting from mergers - are tracked until they interact and merge with other ejecta. The ejecta lose internal energy via adiabatic losses when propagating outwards. However, during mergers, a fraction of their kinetic energy is converted into internal energy. The details of the physics and the description of the main parameters of the model are presented in the original paper. The aim of this study is to investigate the

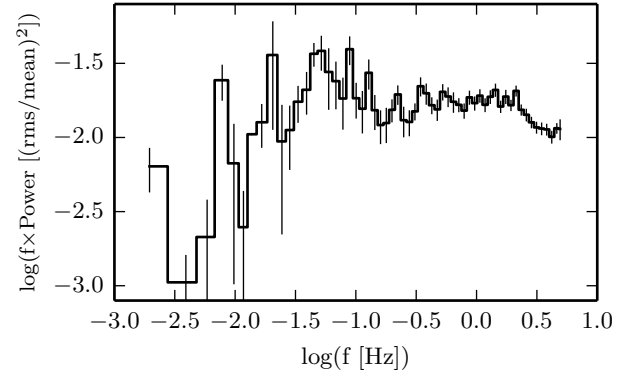


Figure 1. X-ray power spectral density (PSD) of GX 339-4 in the 3-20 keV band, used to constrain the fluctuations of the bulk Lorentz factor of the ejecta. The PSD was extracted for the *RXTE* PCA observations with ObsId 95409-01-09-03 which was quasi-simultaneous with *WISE* (goodtime exposure ~ 1360 s). Standard procedures were used for computing the PSD (for details, see section 4.2 of Gandhi et al. (2010)).

possibility to reproduce GX 339-4 broad-band spectra and infrared light curves measured in Gandhi et al. (2011) with such a jet model, using the X-ray PSD as input for the fluctuations of the bulk Lorentz factor γ of the jet.

Following Gandhi et al. (2011), we take as initial parameters representative of the source, a mass of the central object of $10 M_{\odot}$ and a distance of 8 kpc (Zdziarski et al. 2004; Shidatsu et al. 2011). We let our simulations run for $t_{simu} = 10^5$ s (~ 1 day), to allow the jet to develop. Due to the uncertainty on the inclination angle θ , we examine different values between 20 and 50 degrees. We set the jet opening angle ϕ to 1° . We simulate a counter-jet in this study. However, its contribution to the total spectral energy distribution is less than 10% in the energy range of interest.

The total power available to the jet is an important parameter of the model. To estimate that parameter, we follow the method described in Kording et al. (2006) and use equation (6) and equation (8) of this paper to relate the observed X-ray luminosity of an X-ray binary source to the power available to its jets:

$$P_{jet} \approx 1.57 \times 10^{37} \left(\frac{L_{2-10\text{keV}}}{10^{36}\text{ergs}^{-1}} \right)^{0.5} \text{ erg/s} \quad (1)$$

Gandhi et al. (2011) reports an X-ray luminosity during the observations of $L_{2-10\text{keV}} = 2.0 \times 10^{37}\text{ergs}^{-1}$. As a consequence, we estimate the total power of the jet during the observations to be $P_{jet} \simeq 0.05 L_{Edd}$.

Finally, the most important parameter of our model is the distribution of the fluctuations of the jet's bulk Lorentz factor. We choose for the distribution of the fluctuations of the kinetic energy $\gamma - 1$ to follow the shape of GX 339-4 quasi-simultaneous X-ray PSD, observed by *RXTE* and shown in Fig. 1, as X-ray PSD is thought to trace the variability of the accretion flow in X-ray binary sources. Moreover the fractional rms amplitude of $\gamma - 1$ is set to be equal to that of the X-ray PSD, in this case 35.6%. By imposing the distribution of the fluctuations of the jet's bulk Lorentz factor to follow the X-ray PSD, we connect the physics of the jets to the variability of the inner part of the accretion flow.

Table 1. Parameters explored

Parameters	Range of values
Inclination angle, θ	20°, 30°, 40°, 45°, 50°
Mean Lorentz factor, γ_{mean}	1.5, 2, 4
Electron equipartition, ξ_e	0.5, 1
Proton equipartition, ξ_p	0, 0.5, 1
Ejecta scheme	constant shell kinetic energy, constant shell mass, random shell mass
Shock propagation scheme	slow, fast

In order to find the preferred set of parameters which reproduces correctly the broad-band spectra of the source, we have investigated the following parameters of the model: the mean jet Lorentz factor γ_{mean} , the electron and proton equipartition factors ξ_e and ξ_p , the ejecta scheme, and the shock propagation scheme. γ_{mean} sets the amplitude of the overall spectra. The model provides three methods to generate the ejected shells: the ejecta have either a constant kinetic energy, or a constant mass, or their masses randomly vary, following the same distribution as the Lorentz factor's fluctuations. The ejecta scheme with constant shell mass provides the most pronounced bimodal behaviour of the correlation coefficients as observed by Gandhi et al. (2011). Therefore, we impose that scheme for the rest of the study. Finally the shock propagation scheme is a parameter representing the two treatments available in the model of the energy dissipation occurring during a merger: a slow dissipation method, which overestimates the energy dissipation time, and a fast dissipation method, which underestimates the dissipation time-scale. These parameters, and their range, are listed in Table 1.

To assess the correctness of our models in reproducing the spectral and timing observations of GX 339-4, we compared the simulated spectral energy distributions and infrared light curves to the data. The spectral and timing analyses performed and the results obtained are presented in the following sections.

3 SPECTRAL ANALYSIS

We use the internal shock model to generate different scenarios of jet formation and emission. The emission process considered in the model is solely synchrotron self-absorbed from non-thermal electrons. The electron distribution is a power-law of spectral index $p = 2.3$, with its minimum and maximum energies (γ_{min} and γ_{max}) set arbitrarily and fixed throughout the simulation. The choice of $p = 2.3$ is driven empirically by the observed slope of the infrared spectrum interpreted as optically thin synchrotron radiation by a power-law energy distribution of electron (see Gandhi et al. 2011). This value of p is moreover consistent with typical value expected in shock acceleration. The emission from every shell, initially injected as well as products of mergers, is calculated. The final SED, being compared to the data, is the time-average of all these individual emissions over the simulation running time t_{simu} . The broad-band spectra are computed from 10^7 to 10^{16} Hz.

It is important to note that the general shape of the simulated SED is determined solely by the shape of the PSD

used as an input to the fluctuations of the jet Lorentz factor. The explored parameters only allow to modify the flux normalisation or shift it in the photon frequency direction. Moreover these parameters are degenerated, as two different sets of parameters can produce similar spectra. Hence, reproducing the overall shape of a observed spectra depends essentially on the shape imposed to the fluctuations of the jet's bulk Lorentz factor.

Fig. 2 compares our preferred model spectral energy distribution to the broad-band spectra of GX 339-4. The finding of this preferred set of parameters is done by an approximate match of the radio-to-infrared data. Despite the fact that no quantitative statistical fit has been carried out on the SED, we calculate a reduced- χ^2 of 1.19 for 8 degrees of freedom (9 data points: two radio points, four *WISE* data points and the first three optical/ultraviolet (OUV) points, and 1 free parameters: inclination angle) for this particular set of parameters. When we do not consider the presence of a counter-jet, the reduced- χ^2 lowers to 0.80. The significant difference in the reduced- χ^2 values is mainly due to the higher contribution of the counter-jet to the radio points ($\sim 10\%$) compared to its contribution in the *WISE* bands ($\sim 1\%$). 5 of the 9 data points used in the calculation of the reduced- χ^2 do not include information on their variability over time. Consequently, the reduced- χ^2 does not take into account the variance of flux in its calculation but only the error on each observed measurement. Taking into account the flux variability of the 4 *WISE* data points would decrease their contribution to the reduced- χ^2 by roughly a factor 2 and therefore would decrease as well the resulting reduced- χ^2 . It is apparent from this figure that we are capable of reproducing the overall shape of the radio-to-infrared observations with an internal shock model of jets powered with the accretion flow variability of the source. One should note that the OUV emissions are believed to originate from the outer parts of the accretion flow. We do not attempt to model this region. Finally, we do not model the X-ray emission that we attribute to the accretion flow. Instead we use the X-ray emission as an upper limit to define the feasibility of our fit. We discuss the possible contribution of the jet to X-ray emission in Section 5.

The small discrepancy between the radio data points and our model can be partially explained by the fact that the radio observations were not performed simultaneous with *WISE* observations. In fact, if we use only the radio flux of the observation closest to the *WISE* observations (on 2010 March 14) instead of the mean of the two observations, then the model lies within the error bars of the radio points. The conical geometry assumed for the jet in this work may have an impact on the radio emission as well.

Table 2 presents the parameters of our preferred model. In bold are the parameters of the model, explored in our study. These parameters are consistent with the current knowledge we have on GX 339-4. However due to the degenerate nature of the parameters, this fit is not unique. Nevertheless, the result does provide strong hints on the physical processes happening within the jets and its connexion to the accretion flow variability.

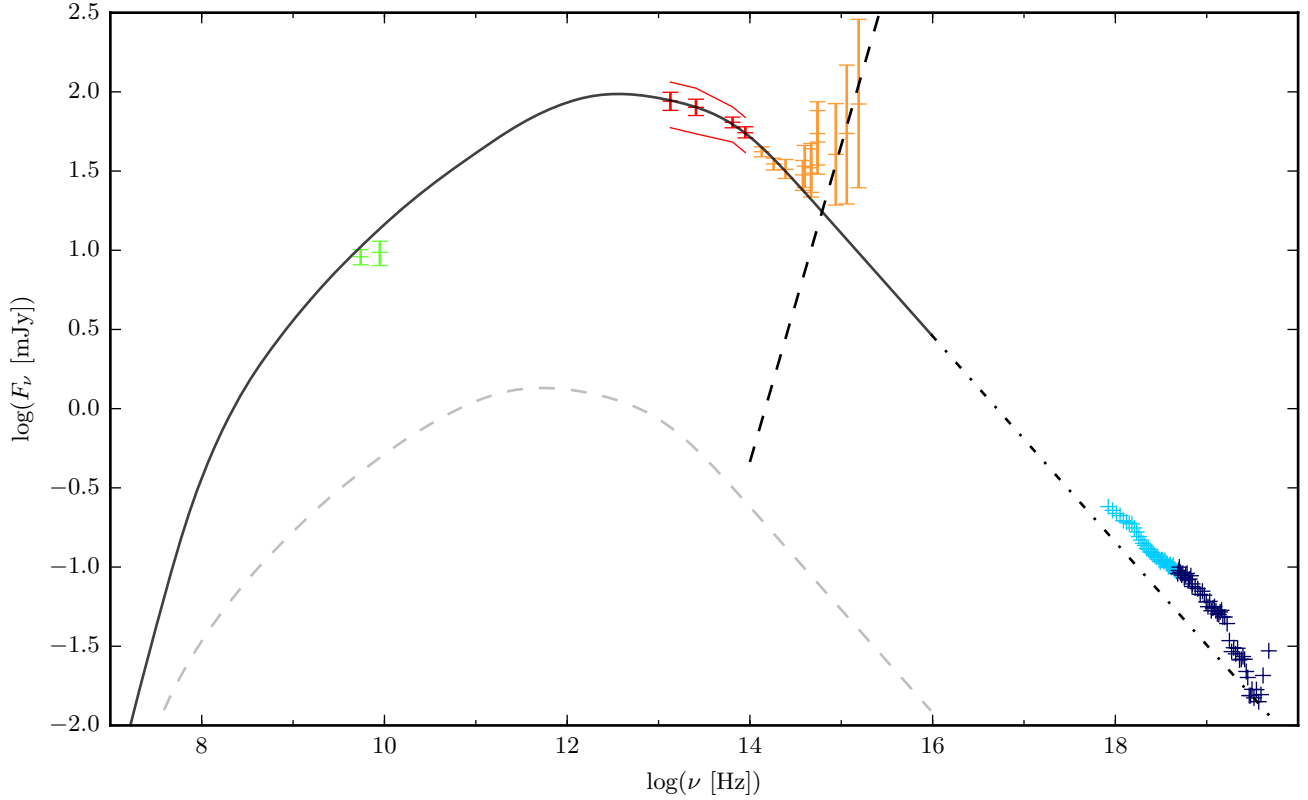


Figure 2. Broadband spectra of our preferred model. Data points are from Gandhi et al. (2011). Radio points are plotted in green, *WISE* data in red, the near-infrared, optical and ultraviolet in orange and the X-ray in blue. The radio points were obtained during two days, closest to but not simultaneous with *WISE* observations. The error bars represent the statistical and systematic errors on the mean. The total synchrotron self-absorbed jet emission from our model is shown as the solid black line. The contribution of the counter-jet is represented by the dashed grey line. Red curves represent the rms amplitude of variability over the 13 *WISE* epochs. The spectra have been averaged over the whole duration of the simulation. The dashed and dot-dashed black lines represent the contribution from the accretion disk to the spectra and the extrapolation of the optically thin synchrotron jet's emission, respectively. X-ray emission is used here solely as upper limits to define the feasibility of our fit.

Table 2. Preferred model parameters

Parameters	Values
M_{bh}	$10 M_{\odot}$
t_{simu}	10^5 s
r_{dyn}	$10 r_G$
Δt	9.941 ms
ϕ	1°
f_{volume}^a	0.7
γ_a^b	4/3
γ_{mean}	2
PSD shape & amplitude	GX 339-4 X-ray PSD (see Fig. 1)
Ejecta scheme	constant shell mass
P_{jet}	$0.05 L_{Edd}$
ξ_e	1
ξ_p	0
p^c	2.3
γ_{min}	1
γ_{max}	10^6
θ	23°
Shock propagation scheme	fast

^a volume filling factor of the colliding shells

^b effective adiabatic index of the flow

^c spectral index of the electron distribution

4 TIMING ANALYSIS

Following the finding of a preferred set of parameters, we compute the light curves of our preferred-model on time-scale of 11 seconds, at four infrared frequencies corresponding to the frequencies of *WISE* bands.

One important point should be noted here. On one hand, the internal shock jet model produces full light curves, from the beginning of the simulation to the end. On the other hand, *WISE* satellite produces a sampling of 11-second scans, at multiples of the satellite orbital period of 95 minutes. To enable a comparison between the simulations and the data, one needs to apply a mask reproducing the *WISE* scan of the source on the simulated light curves. By doing so, we obtain a set of 13-points light curves comparable to data.

To perform the comparison of our simulated light curves to data, we examine three characteristics: the average flux F_ν and the fractional variability amplitudes F_{var} of the light curves, in each of the *WISE* infrared bands W_i , as well as the correlation coefficients R of fluxes between these bands. For a light curve consisting of N fluxes F_ν^j measured at discrete

times t_j , F_{var} is defined as follows:

$$F_{var} = \sqrt{\frac{S^2}{F_{\nu}^2}} \quad (2)$$

$$\text{with } S^2 = \frac{1}{N-1} \sum_{j=1}^N (F_{\nu}^j - F_{\nu})^2 \quad (3)$$

The correlation coefficients R are defined as the covariance of light curves in two bands normalised by the product of the variances in each band.

To take into account the measurement uncertainties in these three characteristics, we used Monte-Carlo bootstrapping to generate from each simulated light curve a collection of noised light curves. The noise added to each of the 13 epochs is drawn from a Gaussian distribution with a standard deviation equal to the errors on the individual *WISE* fluxes.

The infrared light curves are observables of a random variability process specific to the source. The *WISE* observations provides us with one realisation of that process. Whereas the simulations provide us with many realisations, some of which are similar to the observations and some others are not. To determine whether our model statistically reproduces the observations, we investigate the distribution of simulated light curves. To that end, we use two kinds of estimators. As a first estimator, we compute the model distribution for each of the three characteristics F_{ν, W_i} , F_{var, W_i} and $R_{W_i}^{W_j}$.

Fig. 3, Fig. 4 and Fig. 5 present the distributions of F_{ν} , F_{var} and R , respectively, of all the noised simulated light curves of our preferred model. Indicated on the figures by a red arrow is the position of the *WISE* observations within each distribution. In addition, the figure shows in grey area the 68% variation around the median of the distribution, corresponding to a '1- σ ' variation if the distributions were Gaussian. To investigate if the *WISE* observations are typical in the framework of our model (our null-hypothesis), we evaluate the p-value of each observation characteristic. The p-value is the probability of obtaining a test statistic result at least as extreme as the one that was actually observed, assuming that the null hypothesis is true. For the flux and the fractional variability amplitude, the p-values are greater than 0.1 and we cannot reject our null-hypothesis. However, for the correlation coefficients of W4-W2, W4-W1 and W3-W1, the p-values are between 0.01 and 0.05. It suggests that our model does not fully reproduce the correlations seen between the bands with *WISE*. Indeed, the simulated light curves prove to be more deeply correlated than the observations. Nevertheless, it is interesting to note that the evolution of the mean values of the correlation coefficients R in Fig. 5 follows that of the observations. In the model, similar to the observations, bands W4 and W3, as well as W2 and W1 are the most correlated. Whereas W4 and W1 and W4 and W2 are the least correlated. Suggestions to explain the discrepancy in the correlation coefficients between the model and the observations are discussed in Section 5.

Fig. 6 presents a particular set of simulated light curves from our preferred model which have spectral as well as timing properties comparable to the *WISE* observations. That is, the simulated light curves shown here are the ones presenting simultaneously fluxes, variability and correlation co-

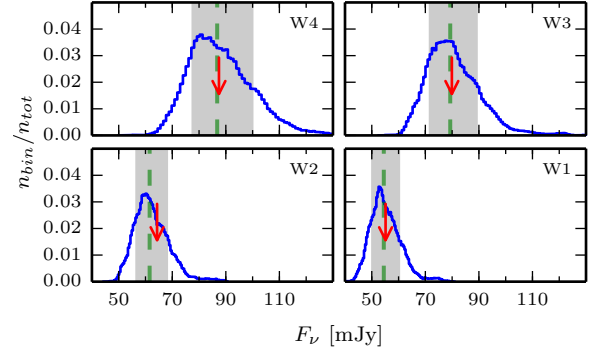


Figure 3. Distribution of F_{ν} . The red arrow indicates the position of the observations. The green dash-line indicates the median of the distribution, the grey area represents the 1- σ variation about the median.

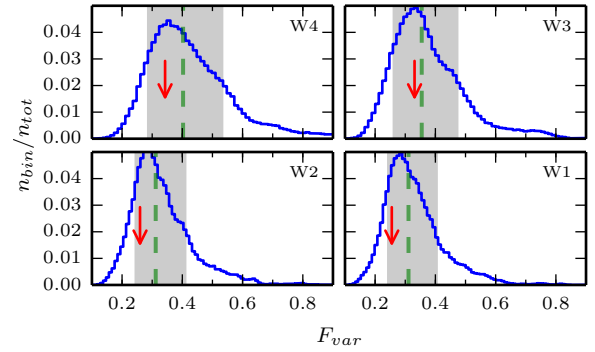


Figure 4. Distribution of F_{var} . The red arrow indicates the position of the observations. The green dash-line indicates the median of the distribution, the grey area represents the 1- σ variation about the median.

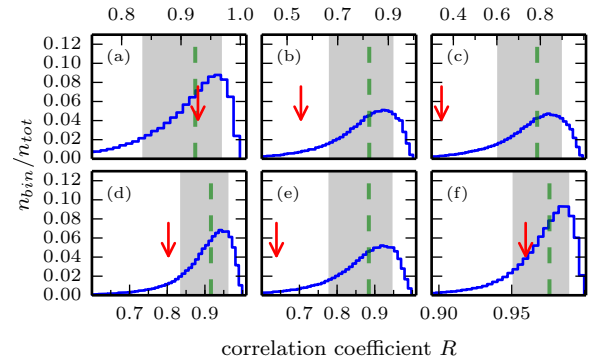


Figure 5. Correlation coefficient distributions of the simulated light curves of our preferred model. Comparing: (a) W4-W3, (b) W4-W2, (c) W4-W1, (d) W3-W2, (e) W3-W1, and (f) W2-W1. The red arrow indicates the position of the observations. The green dash-line indicates the median of the distribution, the grey area represents the 1- σ variation about the median.

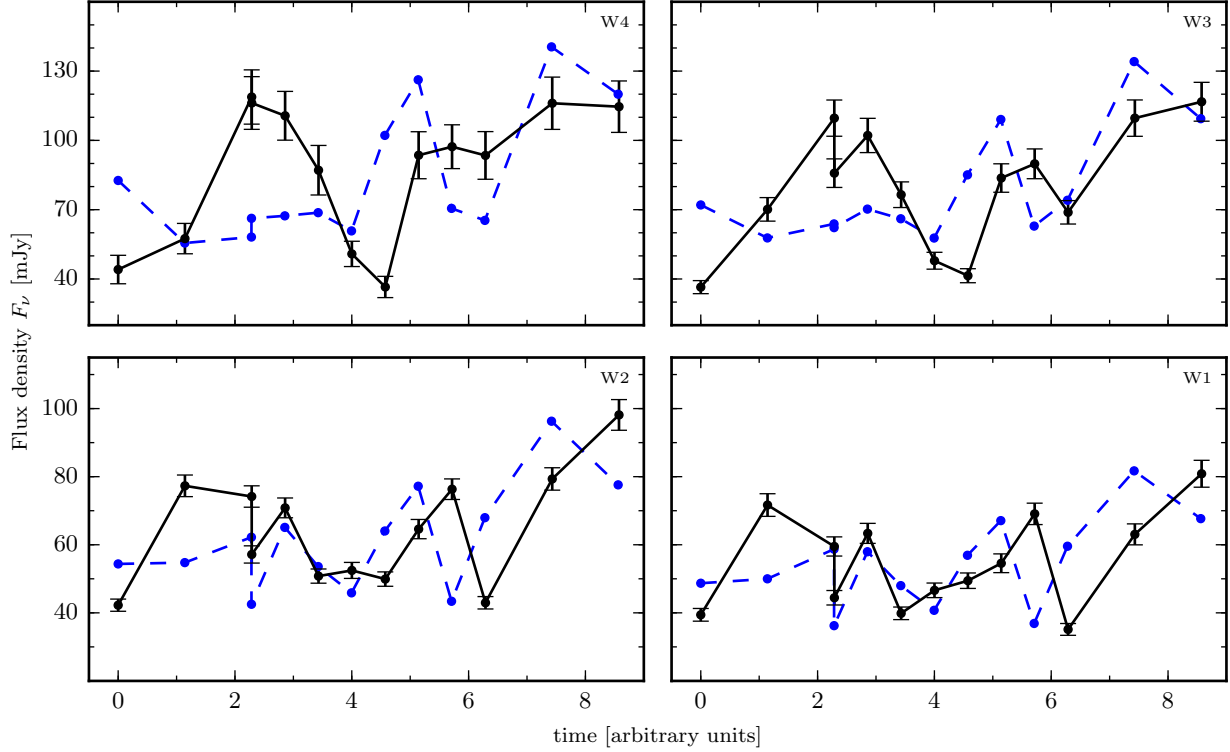


Figure 6. Selected set of light curves reproducing the observations: in blue dash, the simulated light curves, and in black solid, *WISE* light curves from Gandhi et al. (2011). The error bars represent the statistical and systematic errors.

Table 3. Statistics of our preferred set of simulated light curves compared to those of the *WISE* observations.

		simulation	<i>WISE</i>	p-value
F_ν [mJy]	W1	54.63	55.2 ± 3.9	0.45
	W2	61.98	64.3 ± 4.6	0.33
	W3	78.81	79.9 ± 7.3	0.47
	W4	83.41	87.4 ± 8.3	0.47
F_{var}	W1	0.24	0.25 ± 0.03	0.23
	W2	0.25	0.25 ± 0.03	0.24
	W3	0.30	0.32 ± 0.06	0.44
	W4	0.35	0.32 ± 0.06	0.36
R	W4-W3	0.97	0.93	0.47
	W4-W2	0.81	0.55	0.07
	W4-W1	0.76	0.35	0.03
	W3-W2	0.91	0.80	0.10
	W3-W1	0.87	0.64	0.04
	W2-W1	0.99	0.96	0.24

efficients closest to the red arrows indicating in Fig. 3, Fig. 4 and Fig. 5. Table 3 shows the values obtained for F_ν , F_{var} and R of that particular set of simulated light curves and compare them to those reported by Gandhi et al. (2011). In addition, the table reports the exact p-values obtained for each *WISE* characteristic.

The distributions of produced light curves indicate that, taken separately, the variance of each characteristic of our model is reasonably consistent with the observations. However, F_ν , F_{var} and R are correlated variables. Investigating them separately may bias our results. To overcome this bias,

we define, as the second estimator, a quantity which combines all three characteristics, for each noised simulated light curve s and for the observations, as follows:

$$\frac{\chi_s^2}{N} = (\mathbf{X}_s - \langle \mathbf{X}_s \rangle) \cdot (\mathbf{Q} \otimes (\mathbf{X}_s - \langle \mathbf{X}_s \rangle)) \quad (4)$$

$$\frac{\chi_{obs}^2}{N} = (\mathbf{X}_{obs} - \langle \mathbf{X}_s \rangle) \cdot (\mathbf{Q} \otimes (\mathbf{X}_{obs} - \langle \mathbf{X}_s \rangle)) \quad (5)$$

where $N = 8$ or 14 is the number of degrees of freedom, \mathbf{X}_s and \mathbf{X}_{obs} are matrices representing the characteristics - F_ν , F_{var} and R - in all four of *WISE* energy bands for each noised simulated light curves s and for the observations respectively, $\langle \mathbf{X}_s \rangle$ is the mean of \mathbf{X}_s over s , and \mathbf{Q} the inverse of the covariance matrix.

This quantity is similar to a reduced- χ^2 , with one important difference: the distribution of the characteristics are not Gaussian. The χ^2 describes the match between the modelled and observed values of the three characteristics, exactly as it describes the match between the flux at different energies in usual spectral fitting for instance. As the model is intrinsically stochastic, we do not aim at reproducing accurately each single observation. Instead we measure deviation of the observations to the model by comparing the statistical properties of those. As these characteristics are likely to be correlated, we use the inverse \mathbf{Q} of the covariance matrix to compute the χ^2 rather than using the simpler expression for independent variables.

Fig. 7 presents two distributions of that quantity. On one hand, the reduced- χ^2 was calculated considering the av-

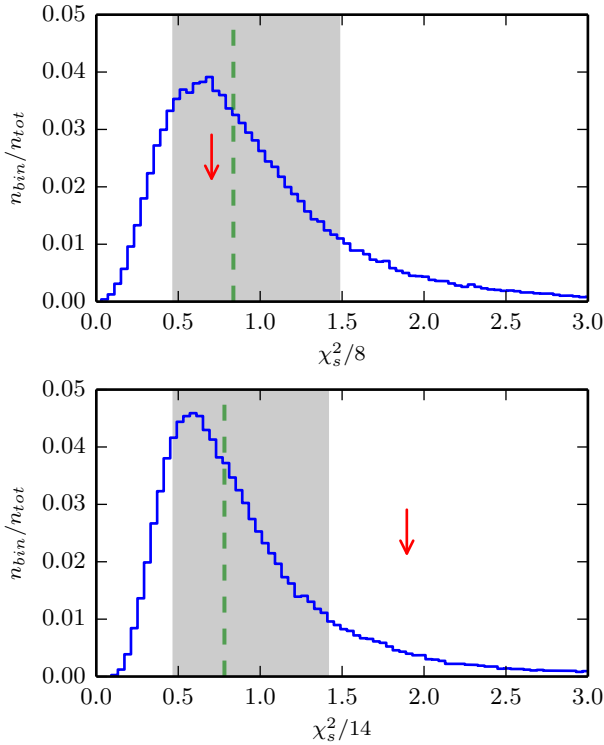


Figure 7. Distributions of reduced- χ^2_s : (top) considering F_ν and F_{var} only; (bottom) considering F_ν , F_{var} and R . The red arrow indicates the position of the corresponding reduced- χ^2_{obs} . The green dash-line indicates the median of the distribution, the grey area represents the $1-\sigma$ variation about the median.

erage flux and the fractional variability amplitudes only (top panel). On the other hand, it was calculated also including the correlation coefficients (bottom panel). The reduced- χ^2 of the observations (represented by the red arrow) is equal to 0.71 and 1.89, respectively. The discrepancy between the model and the observations regarding the correlation coefficients reflects in the relatively high reduced- χ^2_{obs} obtained when considering all three characteristics in its calculation. Alternatively, the lower reduced- χ^2_{obs} , obtained when considering F_ν and F_{var} only, suggests that our model correctly reproduces the spectral and timing properties of the source at the time of the observations but does not reproduce the correlated nature of the bands. The p-values obtained for each case (0.38 and 0.08, respectively) suggest a similar conclusion.

5 DISCUSSION

The present work was designed to study the connexion between the inner part of an accretion flow and the base of the corresponding launched outflow, in X-ray binary sources in the hard state. Using *WISE* observations of GX 339-4 on 2010 March 11 as a test-case, the results of this investigation show that it is indeed possible to reproduce simultaneously broad-band spectral and timing observations of a X-ray binary source in the hard state with an internal shock jet model. The required condition is to use the X-ray timing information provided by the corresponding power spectral density as an input to the fluctuations of the bulk Lorentz

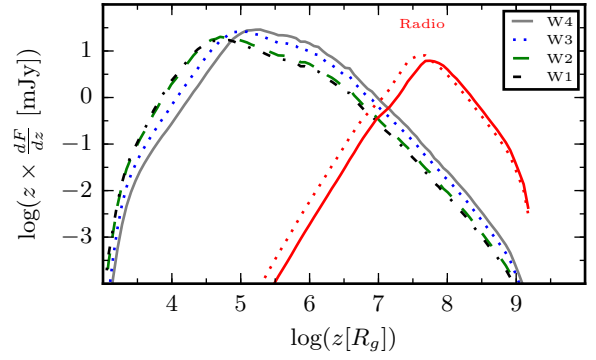


Figure 8. Regions of emission in the infrared and radio bands. In red, are the radio emission at 5.5 GHz (solid) and 9 GHz (dot). In solid black, dot blue, dash green and dot-dash black are the infrared emission in W4, W3, W2 and W1 bands, respectively.

factor γ . This finding corroborates the ideas of Jamil et al. (2010) and Malzac (2014), who suggested that accretion flow variability, traced by X-ray timing information, could drive internal shock in jets.

Another point that could be investigated to characterise the disc-jet connexion is the jet's contribution to the X-ray variability. Emission produced by the model at frequencies higher than 10^{16} Hz are currently extrapolated from the optically thin synchrotron power-law tail. However several cooling processes, such as synchrotron self-Compton or inverse-Compton of the disc emission for example, are not considered in the model yet. Moreover, the form as well as the maximum energy of the emitting particle distribution are currently being fixed and arbitrarily set throughout the simulation. These restrictions lead to the choice of neglecting the possible contribution of the jet to the X-ray variability in the present state of the model.

Despite the more pronounced correlation in the simulated light curves compared to the observations, it is interesting to note the evolution of the spreading of the correlation coefficients R in Fig. 5 follows that of the observations. This tendency may be explained in terms of regions of emission. Fig. 8 illustrates this trend by showing that the regions of peak emission of W1 and W2 on one hand, and W3 and W4 on the other hand, are closely located, while the regions of peak emission of W1 and W4 are the most distant to each other. We may improve the correspondence between the correlation coefficients of the model and the observations by increasing the contribution of the counter-jet to the overall emission. This is done by releasing the constraint on the value of P_{jet} and increasing the inclination angle to 50° . We find a new fit to the SED by setting P_{jet} to $0.14 L_{Edd}$. However that new choice of parameters does not enhance the overall fit (new reduced- χ^2 is equal to 4.17) and ameliorates only slightly the correspondence between the correlation coefficients of the model and the observations.

The stronger correlation coefficients seen in the model, compared to those of the observation, is due to the regions of peak emission being so close to each others that a fluctuation occurring in one band does not have the time to be totally dissipated before arriving in the emitting region of the next band. To reduce the correlation between bands, one would need to allow the particles to cool on a faster timescale

or over a longer period of time. Improving the modelling of the particle distribution by taking into account radiative processes or modifying the geometry of the jet to consider amplified radial expansion at the shock lead by an increase of the internal pressure and possible radial contractions in between shock regions may adapt the cooling timescale to that needed. Similarly, modifying the scale of the dissipation profile along the jet by changing the one-to-one relation between the accretion flow variability and the ejecta velocity distribution used in this study may provide a solution to that issue.

Nevertheless, it is important to note that this disagreement between the observed and modelled correlation coefficients does not challenge internal shocks as a dissipation process occurring in astrophysical jets. Such disagreement would appear in any model using any other dissipation process, as long as they also assume a jet of conical geometry and similar radiative treatment. Overall, investigating the variable properties of our model, improving the modelling of the particle distribution or modifying the geometry of the jet will shed some light on the origin of that dichotomy and will help to understand even better the deep relation between accretion and ejection processes in accreting black holes.

To conclude, this work is a step forward toward revealing the details of the accretion-ejection process in accreting black hole systems. The results of this study indicate that the conversion of jet kinetic energy to internal energy through internal shocks may well be the dissipation process needed to compensate for the adiabatic losses in conical compact jets. Furthermore, the results of this work support the idea of the importance of the X-ray variability on jet emission strength. A recent study by Dinçer et al. (2014) corroborates this idea. They observed that the standard sources in the radio/X-ray luminosity relation show stronger broadband X-ray variability than outliers at a given X-ray luminosity. Further radio, mid-infrared and X-ray timing observations will provide better constraints to the accretion-ejection connexion and to the present model. In addition, understanding and being able to reproduce the spectral, timing and correlation properties of a source will allow the model to provide useful predictions to future observations, with information such as at which frequency one can expect to observe maximum jet variability or at which timescale is the best for probing it.

ACKNOWLEDGEMENTS

J.M. thanks the Institute of Astronomy (Cambridge) for hospitality. P.G. acknowledges support from STFC (grant reference ST/J003697/1). The authors are grateful to the anonymous referee for his/her helpful comments on the manuscript. This work is part of the CHAOS project ANR-12-BS05-0009 supported by the French Research National Agency (<http://www.chaos-project.fr>).

REFERENCES

- Blandford R. D., Königl A., 1979, *ApJ*, 232, 34
 Böttcher M., Dermer C. D., 2010, *ApJ*, 711, 445
 Cadolle Bel M. et al., 2011, *A&A*, 534, A119
 Casella P. et al., 2010, *MNRAS*, 404, L21
 Corbel S., Coriat M., Brocksopp C., Tzioumis A. K., Fender R. P., Tomsick J. A., Buxton M. M., Bailyn C. D., 2013, *MNRAS*, 428, 2500
 Corbel S., Fender R. P., 2002, *ApJL*, 573, L35
 Corbel S., Fender R. P., Tzioumis A. K., Nowak M., McIntyre V., Durouchoux P., Sood R., 2000, *A&A*, 359, 251
 Corbel S., Nowak M. A., Fender R. P., Tzioumis A. K., Markoff S., 2003, *A&A*, 400, 1007
 Daigne F., Mochkovitch R., 1998, *MNRAS*, 296, 275
 Dinçer T., Kalemci E., Tomsick J. A., Buxton M. M., Bailyn C. D., 2014, *ApJ*, 795, 74
 Done C., Diaz Trigo M., 2010, *MNRAS*, 407, 2287
 Dunn R. J. H., Fender R. P., Körding E. G., Cabanac C., Belloni T., 2008, *MNRAS*, 387, 545
 Fender R. P., Hanson M. M., Pooley G. G., 1999, *MNRAS*, 308, 473
 Fender R. P., Pooley G. G., Durouchoux P., Tilanus R. P. J., Brocksopp C., 2000, *MNRAS*, 312, 853
 Fender R. P., Spencer R. E., Newell S. J., Tzioumis A. K., 1997, *MNRAS*, 286, L29
 Gandhi P., 2009, *ApJL*, 697, L167
 Gandhi P. et al., 2011, *ApJL*, 740, L13
 Gandhi P. et al., 2010, *MNRAS*, 407, 2166
 Gandhi P. et al., 2008, *MNRAS*, 390, L29
 Hynes R. I., Steeghs D., Casares J., Charles P. A., O'Brien K., 2003, *ApJL*, 583, L95
 Hynes R. I., Steeghs D., Casares J., Charles P. A., O'Brien K., 2004, *ApJ*, 609, 317
 Jamil O., Fender R. P., Kaiser C. R., 2010, *MNRAS*, 401, 394
 Kaiser C. R., Sunyaev R., Spruit H. C., 2000, *A&A*, 356, 975
 King A. R., Pringle J. E., West R. G., Livio M., 2004, *MNRAS*, 348, 111
 Körding E. G., Fender R. P., Migliari S., 2006, *MNRAS*, 369, 1451
 Lyubarskii Y. E., 1997, *MNRAS*, 292, 679
 Malzac J., 2013, *MNRAS*, 429, L20
 Malzac J., 2014, *MNRAS*, 443, 299
 Markoff S., Nowak M., Corbel S., Fender R., Falcke H., 2003, *A&A*, 397, 645
 Mayer M., Pringle J. E., 2006, *MNRAS*, 368, 379
 Miller J. M., Homan J., Steeghs D., Rupen M., Hunstead R. W., Wijnands R., Charles P. A., Fabian A. C., 2006, *ApJ*, 653, 525
 Motch C., Ilovaisky S. A., Chevalier C., 1982, *A&A*, 109, L1
 Muñoz-Darias T., Casares J., Martínez-Pais I. G., 2008, *MNRAS*, 385, 2205
 Rees M. J., 1978, *MNRAS*, 184, 61P
 Rees M. J., Meszaros P., 1994, *ApJL*, 430, L93
 Shidatsu M. et al., 2011, *PASJ*, 63, 785
 Spada M., Ghisellini G., Lazzati D., Celotti A., 2001, *MNRAS*, 325, 1559
 Wright E. L. et al., 2010, *AJ*, 140, 1868
 Zdziarski A. A., Gierliński M., Mikołajewska J., Wardziński G., Smith D. M., Harmon B. A., Kitamoto S., 2004, *MNRAS*, 351, 791

This paper has been typeset from a \LaTeX file prepared
by the author.